Available online at www.sciencedirect.com
ScienceDirect
Journal of Computational Physics 219 (2006) 391–403
JOURNAL OF COMPUTATIONAL PHYSICS
www.elsevier.com/locate/jcp

A multi-dimensional upwind scheme for solving Euler and Navier–Stokes equations

Yu-Xin Ren *, Yutao Sun

Department of Engineering Mechanics, Tsinghua University, Qinghuayuan, Beijing 100084, PR China

Received 21 December 2004; received in revised form 17 February 2006; accepted 23 March 2006
Available online 2 May 2006

Abstract

This paper presents a multi-dimensional upwind finite volume scheme for solving the gasdynamic Euler and Navier–Stokes equations. In evaluating the inviscid numerical fluxes, the full governing equations are solved on every cell interface to account for the multi-dimensional effects. To make the scheme efficient, the governing equations are solved on every cell interface using an operator splitting method: in the first step, the contribution of inviscid terms is modeled by solving the linearized Euler equations in characteristic form; in the second step, the contribution of viscous terms are included by a simple correction procedure. The resulted scheme is efficient and easy to be applied on general control volumes. Several numerical test cases are presented to verify the proposed scheme.

MSC: 65M06; 76N15; 35L65

Keywords: Multi-dimensional upwind scheme; Finite volume scheme; Euler equations; Navier–Stokes equations; Reconstruction

1. Introduction

In recent years, there have been considerable efforts to develop so called "genuinely multi-dimensional schemes" for solving hyperbolic conservation laws. These schemes are motivated by various considerations and expectations, such as improving the stability [3] and resolution properties [10], facilitating the applications for some specific problems [3,9], and cure the deficiencies [13] of more traditional methods for solving multi-dimensional problems such as the dimensional splitting finite difference schemes and the "grid-aligned" finite volume schemes [15]. Since mid-1980s, there have been a number of proposals on the construction of genuinely multi-dimensional schemes, which include: (1) the fluctuation-splitting schemes for the equations of gasdynamics developed by Roe [4], Deconinck et al. [4], van Leer [19], and many others; (2) the corner transport upwind (CTU) scheme proposed by Colella [3]; (3) the wave propagation algorithm for multi-dimensional systems of conservation laws presented by Le Veque [8,9]; (4) the weighted-average-flux (WAF) scheme of Billet

* Corresponding author. Tel.: +86 10 62785543; fax: +86 10 62781824.
E-mail address: ryx@tsinghua.edu.cn (Y.-X. Ren).

0021-9991/$ - see front matter
doi:10.1016/j.jcp.2006.03.018

and Toro [1]; (5) the method of transport (MoT) of Fey [6] which has been improved to MoT-ICE by Noelle [11]; (6) the finite volume evolution Galerkin (FVEG) methods developed by Lukáčová-Medvid'ová et al. [10]; (7) the two-dimensional multi-state linear Riemann solver proposed by Brio et al. [2]; and (8) the multi-dimensional central scheme of Kurganov et al. [7]. This list is by no means exhaustive, many related works can be found in the references therein.

Despite the advantages of these genuinely multi-dimensional schemes mentioned above, many of them are very complex, computationally expensive, and/or currently applicable only on rectangular meshes. The applications of these schemes to solve the compressible Navier–Stokes equations are rare. The goal of the present paper is therefore to develop a multi-dimensional finite volume scheme for solving gasdynamic equations which satisfies the following requirements:

(1) The scheme must be efficient, which means that the cost of the present scheme is comparable to or only slightly lager than the dimensional splitting finite difference schemes and the grid-aligned finite volume schemes.
(2) The scheme must be simple enough to be applied on general shape control volumes in both two and three dimensions.
(3) The scheme can be applied to solve the Euler as well as the Navier–Stokes equations.

The "building block" of the present method is to compute the numerical fluxes on cell interfaces by solving full governing equations instead of their augmented one-dimensional counterparts as being done in the grid-aligned finite volume schemes [18]. The present finite volume scheme is quite similar in spirit to the corner transport upwind (CTU) scheme proposed by Colella [3] as well as the wave propagation algorithm of Le Veque et al. [9]. However, our method is more efficient than these methods by adopting the operator splitting method and a linear solver in characteristic form when updating the dependent variables on cell interface. Another feature of the present scheme is the inclusion of the viscous contribution when evaluating the inviscid fluxes of the Navier–Stokes equations. In this way, the multi-dimensional effects due to the viscous fluxes can be also considered and the resulted scheme is second order accurate in smooth regions. The present method can be applied on general shape control volumes for both structured and unstructured grids. In this paper, only the two-dimensional problems are considered although it is straightforward to extend the present method to three-dimensional cases.

This paper is organized as follows. In Section 2, the present finite volume scheme is presented and the two-dimensional reconstruction procedure is introduced. In Section 3, the central part of the present paper, the algorithm for evaluating the inviscid numerical fluxes is proposed and discussed. In Section 4, we present some numerical test cases for both inviscid and viscous flow problems. And the conclusions are given in Section 5.

2. The finite volume scheme

2.1. The governing equations

We consider the two-dimensional Navier–Stokes equations describing the flow of compressible viscous fluid. In conservation form the equations are

$$\frac{\partial \mathbf{U}}{\partial t}+\frac{\partial \mathbf{F}^{(E)}}{\partial x}+\frac{\partial \mathbf{G}^{(E)}}{\partial y}=\frac{\partial \mathbf{F}^{(V)}}{\partial x}+\frac{\partial \mathbf{G}^{(V)}}{\partial y}, \tag{1}$$

where $\mathbf{U}$ is the vector of the conserved variables given as $\mathbf{U}=[\rho,\rho u,\rho v,\rho E]^{\mathrm{T}}$. The detailed formulations of the flux terms are well known and are omitted here for brevity. This set of equations are closed by the equation-of-state of ideal gas

$$p=(\gamma-1)\rho\left[E-\frac{u^2+v^2}{2}\right].$$

The Euler equations can be considered as a special case of the Navier–Stokes equations in which the coefficient of viscosity is set to zero.

2.2. The finite volume scheme

We consider some two-dimensional domain in x–y space and assume that it is discretized into structured quadrilateral control volumes. Examples of typical control cells are shown in Fig. 1. Finite volume schemes for Eq. (1) are obtained by considering the control volume balance equation

$$\int\int_{\Omega_{ij}} (\mathbf{U}^{n+1} - \mathbf{U}^{n})\,\mathrm{d}x\,\mathrm{d}y + \int_{t_n}^{t_{n+1}} \oint_{\partial\Omega_{ij}} \left(\mathbf{F}^{(E)}\mathbf{i} + \mathbf{G}^{(E)}\mathbf{j}\right)\cdot\mathbf{n}\,\mathrm{d}l\,\mathrm{d}t = \int_{t_n}^{t_{n+1}} \oint_{\partial\Omega_{ij}} \left(\mathbf{F}^{(V)}\mathbf{i} + \mathbf{G}^{(V)}\mathbf{j}\right)\cdot\mathbf{n}\,\mathrm{d}l\,\mathrm{d}t, \tag{2}$$

where $\Omega_{i,j}$ is the control volume, $\partial\Omega_{i,j}$ is the boundary of $\Omega_{i,j}$, $\mathbf{n} = n_x\mathbf{i} + n_y\mathbf{j}$ is the outward unit vector normal to the surface $\partial\Omega_{i,j}$. On a quadrilateral control volume with its faces denoted by I_k $(k = 1,\ldots,4)$, the finite volume scheme can be written as

$$\left(\overline{\mathbf{U}}_{ij}^{n+1} - \overline{\mathbf{U}}_{ij}^{n}\right)\overline{\Omega}_{i,j} + \sum_{k=1}^{4}\int_{t_n}^{t_{n+1}}\int_{I_k} \left(\mathbf{F}^{(E)}\mathbf{i} + \mathbf{G}^{(E)}\mathbf{j}\right)\cdot\mathbf{n}\,\mathrm{d}l\,\mathrm{d}t = \sum_{k=1}^{4}\int_{t_n}^{t_{n+1}}\int_{I_k} \left(\mathbf{F}^{(V)}\mathbf{i} + \mathbf{G}^{(V)}\mathbf{j}\right)\cdot\mathbf{n}\,\mathrm{d}l\,\mathrm{d}t, \tag{3}$$

where $\overline{\mathbf{U}}_{ij}^{n}$ is the average of $\mathbf{U}$ inside $\Omega_{i,j}$ defined by

$$\overline{\mathbf{U}}_{i,j}^{n} = \frac{\int\int_{\Omega_{i,j}} \mathbf{U}^{n}\,\mathrm{d}x\,\mathrm{d}y}{\overline{\Omega}_{i,j}}, \quad \overline{\Omega}_{i,j} = \int\int_{\Omega_{i,j}} \mathrm{d}x\,\mathrm{d}y. \tag{4}$$

In this paper, we are interested in the finite volume scheme that is at most second order accurate. Therefore, it is sufficient to integrate the flux terms in Eq. (3) by using the midpoint rule. Therefore we have

$$\frac{\left(\overline{\mathbf{U}}_{ij}^{n+1} - \overline{\mathbf{U}}_{ij}^{n}\right)}{\Delta t} + \frac{1}{\overline{\Omega}_{i,j}}\left[\sum_{k=1}^{4}\left(\boldsymbol{\Psi}_{k}^{(E)^{\left(n+\frac{1}{2}\right)}}\Delta l_k\right) - \sum_{k=1}^{4}\boldsymbol{\Psi}_{k}^{(V)^{\left(n+\frac{1}{2}\right)}}\Delta l_k\right] = 0, \tag{5}$$

where Δl_k is the length of I_k interface, and the inviscid and viscous numerical fluxes are defined by

$$\boldsymbol{\Psi}_{k}^{(E)^{\left(n+\frac{1}{2}\right)}} = \boldsymbol{\Psi}_{k}^{(E)}\left(\mathbf{U}_{k}^{n+1/2}\right) = \mathbf{H}_{k}^{(E)}\left(\mathbf{U}_{k}^{n+1/2}\right)\cdot\mathbf{n}_k$$

and

$$\boldsymbol{\Psi}_{k}^{(V)^{\left(n+\frac{1}{2}\right)}} = \boldsymbol{\Psi}_{k}^{(V)}\left(\mathbf{U}_{k}^{n+1/2}, \left(\frac{\partial\mathbf{U}}{\partial x}\right)_{k}^{n+1/2}, \left(\frac{\partial\mathbf{U}}{\partial y}\right)_{k}^{n+1/2}\right) = \left(\mathbf{H}_{k}^{(V)}\cdot\mathbf{n}_k\right)\left(\mathbf{U}_{k}^{n+1/2}, \left(\frac{\partial\mathbf{U}}{\partial x}\right)_{k}^{n+1/2}, \left(\frac{\partial\mathbf{U}}{\partial y}\right)_{k}^{n+1/2}\right), \tag{6}$$

where the tensors of inviscid and viscous fluxes are defined, respectively, by

$$\mathbf{H}_{k}^{(E)} = \mathbf{F}_{k}^{(E)}\mathbf{i} + \mathbf{G}_{k}^{(E)}\mathbf{j}$$

and

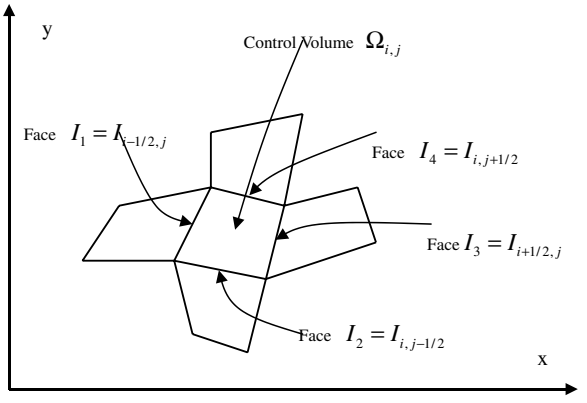

Fig. 1. Typical control volumes for a two-dimensional domain.

$$\mathbf{H}_k^{(V)} = \mathbf{F}_k^{(V)}\mathbf{i} + \mathbf{G}_k^{(V)}\mathbf{j};$$

and $\mathbf{U}_k^{n+1/2}$ is the vector of conservative variables on the midpoint of the interface I_k at

$$t^{n+1/2} = t^n + \frac{\Delta t}{2}.$$

In Section 3, the evaluation of $\mathbf{U}_k^{n+1/2}$ and $\mathbf{\Psi}_k^{(E)^{\left(n+\frac{1}{2}\right)}}$ will be presented in detail, and the contribution of the multi-dimensional effect to the numerical fluxes will also be addressed. To compute the viscous flux $\mathbf{\Psi}_k^{(V)^{\left(n+\frac{1}{2}\right)}}$, it is apparent that $\left(\frac{\partial \mathbf{U}}{\partial x}\right)_k^{n+1/2}$, $\left(\frac{\partial \mathbf{U}}{\partial y}\right)_k^{n+1/2}$ must be evaluated on the midpoint of the interface I_k. This procedure turns out to be cumbersome and computationally expensive. In order to construct an efficient multi-dimensional scheme as we have promised in Section 1, we propose to modify the finite volume scheme, Eq. (5), into a predictor–corrector scheme to account for the viscous effect without evaluating Eq. (6) explicitly. The resulted scheme can be summarized as:

the predictor step

$$\overline{\mathbf{U}}_{ij}^{\overline{n+1}} = \overline{\mathbf{U}}_{ij}^n - \frac{\Delta t}{\overline{\Omega}_{i,j}} \sum_{k=1}^{4} \mathbf{\Psi}_k^{(E)^{\left(n+\frac{1}{2}\right)}} \Delta l_k + \frac{\Delta t}{\overline{\Omega}_{i,j}} \sum_{k=1}^{4} \mathbf{\Psi}_k^{(V)^{(n)}} \Delta l_k; \tag{7}$$

the corrector step

$$\overline{\mathbf{U}}_{ij}^{n+1} = \overline{\mathbf{U}}_{ij}^{\overline{n+1}} + \frac{\Delta t}{2\overline{\Omega}_{i,j}} \sum_{k=1}^{4} \left(\mathbf{\Psi}_k^{(V)^{\overline{(n+1)}}} - \mathbf{\Psi}_k^{(V)^{(n)}} \right) \Delta l_k. \tag{8}$$

It is easy to prove this scheme is second order accurate provided that $\mathbf{U}_k^{n+1/2}$ is evaluated properly using the procedure that will be presented in Section 3. When the Euler equations are considered, Eqs. (7) and (8) will reduce to

$$\overline{\mathbf{U}}_{ij}^{n+1} = \overline{\mathbf{U}}_{ij}^n - \frac{\Delta t}{\overline{\Omega}_{i,j}} \sum_{k=1}^{4} \mathbf{\Psi}_k^{(E)^{\left(n+\frac{1}{2}\right)}} \Delta l_k.$$

The predictor–corrector procedure, Eqs. (7) and (8), for handling viscous terms is new to our knowledge. This procedure can be used in viscous flow computation for many schemes (such as the MoT [6] and the FVEG [10]) that take the transport effect into consideration when computing the cell interface fluxes.

2.3. Reconstruction

In the framework of the finite volume method, at time level $t = t^n$, it is necessary to reconstruct a piecewise polynomial function, $\mathbf{U}(x, y, t^n)$, from the cell average data $\overline{\mathbf{U}}_{i,j}^n$. For a second order scheme, a piecewise linear reconstruction is sufficient. In the present paper, the reconstruction is carried out in terms of primitive variables $\mathbf{W} = (\rho, u, v, p)^{\mathrm{T}}$. When a piecewise linear reconstruction is concerned, we have

$$\mathbf{W}_{i,j}^n = \mathbf{W}^n(x_{i,j}, y_{i,j}) = \overline{\mathbf{W}}_{i,j}^n,$$

where $\overline{\mathbf{W}}_{i,j}^n$ is the vector of the cell averages of primitive variables on control volume $\Omega_{i,j}$ and $\mathbf{W}_{i,j}^n$ is the vector of the primitive variables at the centroid of $\Omega_{i,j}$, i.e., $(x_{i,j}, y_{i,j})$. Therefore, we will not distinguish between $\mathbf{W}_{i,j}^n$ and $\overline{\mathbf{W}}_{i,j}^n$ in the following reconstruction procedure.

In the present reconstruction procedure, we first compute the gradient of primitive variables, $\nabla \mathbf{W}_{i,j}^n$, by

$$\begin{aligned} \nabla \mathbf{W}_{i,j}^n \approx \frac{1}{2\overline{\Omega}_{i,j}} \Big[& L\left(\mathbf{W}_{i+1,j}^n - \mathbf{W}_{i,j}^n, \mathbf{W}_{i,j}^n - \mathbf{W}_{i-1,j}^n\right)\left(\mathbf{n}_{i+1/2,j}\Delta l_{i+1/2,j} - \mathbf{n}_{i-1/2,j}\Delta l_{i-1/2,j}\right) \\ & + L\left(\mathbf{W}_{i,j+1}^n - \mathbf{W}_{i,j}^n, \mathbf{W}_{i,j}^n - \mathbf{W}_{i,j-1}^n\right)\left(\mathbf{n}_{i,j+1/2}\Delta l_{i,j+1/2} - \mathbf{n}_{i,j-1/2}\Delta l_{i,j-1/2}\right) \Big], \end{aligned} \tag{9}$$

where L is the limiter which is chosen as

$$L(a,b)=\frac{\max(ab,0)(a+b)}{a^2+b^2} \tag{10}$$

to suppress the non-physical oscillations near the flow discontinuities. Using this gradient, the piecewise linear reconstruction in $\Omega_{i,j}$ is expressed as

$$\mathbf{W}^n(x,y)|_{(x,y)\in\Omega_{i,j}}=\overline{\mathbf{W}}^n_{ij}+\left(\frac{\partial\mathbf{W}}{\partial x}\right)^n_{i,j}(x-x_{ij})+\left(\frac{\partial\mathbf{W}}{\partial y}\right)^n_{i,j}(y-y_{ij}). \tag{11}$$

3. Genuine multi-dimensional inviscid numerical fluxes

In this section, we will propose a multi-dimensional approach to evaluate the inviscid numerical flux

$$\mathbf{\Psi}_k^{(E)^{\left(n+\frac{1}{2}\right)}}=\mathbf{\Psi}_k^{(E)}\left(\mathbf{U}_k^{n+1/2}\right)=\mathbf{H}_k^{(E)}\left(\mathbf{U}_k^{n+1/2}\right)\cdot\mathbf{n}_k. \tag{12}$$

The central idea of the present approach is to compute $\mathbf{U}_k^{n+1/2}$ at the mid-point of I_k by solving the full Navier–Stokes equations

$$\frac{\partial\mathbf{U}}{\partial t}+\frac{\partial\mathbf{F}^{(E)}}{\partial x}+\frac{\partial\mathbf{G}^{(E)}}{\partial y}=\frac{\partial\mathbf{F}^{(V)}}{\partial x}+\frac{\partial\mathbf{G}^{(V)}}{\partial y} \tag{13}$$

in stead of their augmented one-dimensional counterparts as having been done in the grid-aligned finite volume schemes [18]. In order to construct an efficient multi-dimensional scheme, we solve Eq. (13) using a two step operator splitting method. In the first step, we compute an intermediate value of $\mathbf{U}_k^{n+1/2}$ denoted as $\underset{\frown}{\mathbf{U}}_k^{n+1/2}$ by solving the Euler equations

$$\frac{\partial\mathbf{U}}{\partial t}+\frac{\partial\mathbf{F}^{(E)}}{\partial x}+\frac{\partial\mathbf{G}^{(E)}}{\partial y}=\mathbf{0} \tag{14}$$

using $\mathbf{U}^n$ as initial value. In the second step, $\underset{\frown}{\mathbf{U}}_k^{n+1/2}$ is corrected to get $\mathbf{U}_k^{n+1/2}$ by solving

$$\frac{\partial\mathbf{U}}{\partial t}-\frac{\partial\mathbf{F}^{(V)}}{\partial x}-\frac{\partial\mathbf{G}^{(V)}}{\partial y}=\mathbf{0}. \tag{15}$$

In what follows, we will consider the evaluation of the inviscid numerical flux on interface $I_{i+1/2,j}$ only for simplicity.

3.1. The linearized Euler equations in characteristic form

To evaluate $\underset{\frown}{\mathbf{U}}_{i+1/2,j}^{n+1/2}$, we need not to solve Eq. (14) rigorously. One of the most commonly used practices is to solve a linearized version of Eq. (14). Using the equations in the primitive variable and/or the characteristic variable forms will also facilitate the solution procedures sometimes. In this paper, we use the linearized Euler equations in characteristic form similar to those used in [10]. These equations can be derived as follows.

Referring to Fig. 2, we construct a local coordinate system $(\hat{x},\hat{y})$ where $\hat{x}$-axis is aligned with $\mathbf{n}_{i+1/2,j}$, the outer unit normal vector of interface $I_{i+1/2,j}$. The Euler equations in terms of primitive variables in reference frame $(\hat{x},\hat{y})$ are

$$\hat{\mathbf{W}}_t+\mathbf{A}_1(\hat{\mathbf{W}})\hat{\mathbf{W}}_{\hat{x}}+\mathbf{A}_2(\hat{\mathbf{W}})\hat{\mathbf{W}}_{\hat{y}}=0, \tag{16}$$

where

$$\hat{\mathbf{W}}:=\begin{pmatrix}\rho\\ \hat{u}\\ \hat{v}\\ p\end{pmatrix},\quad \mathbf{A}_1:=\begin{pmatrix}\hat{u}&\rho&0&0\\ 0&\hat{u}&0&\frac{1}{\rho}\\ 0&0&\hat{u}&0\\ 0&\gamma p&0&\hat{u}\end{pmatrix},\quad \mathbf{A}_2:=\begin{pmatrix}\hat{v}&0&\rho&0\\ 0&\hat{v}&0&0\\ 0&0&\hat{v}&\frac{1}{\rho}\\ 0&0&\gamma p&\hat{v}\end{pmatrix}, \tag{17}$$

and

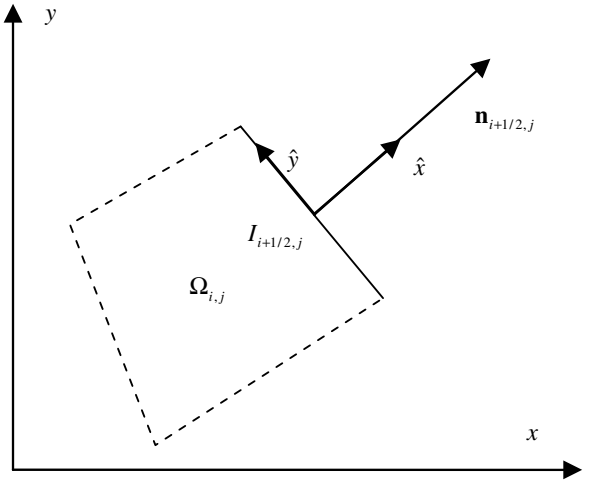

Fig. 2. Local coordinate systems $(\hat{x},\hat{y})$ at interface $I_{i+1/2,j}$. The $\hat{x}$-axis is aligned with $\mathbf{n}_{i+1/2,j}$ and $\hat{y}$-axis is normal to $\mathbf{n}_{i+1/2,j}$.

$$\hat{u} = u\cos\theta + v\sin\theta, \quad \hat{v} = -u\sin\theta + v\cos\theta \tag{18}$$

are the normal and tangential components of the velocity vector, respectively. θ is the angle between $\mathbf{n}_{i+1/2,j}$ and the x-axis, i.e.,

$$\theta = \arccos(\mathbf{n}_{i+1/2,j}\cdot\mathbf{i}).$$

After computing the left and right states of the primitive variables

$$\mathbf{W}^{n,L}_{i+1/2,j} = \mathbf{W}^n(x_{i+1/2,j}, y_{i+1/2,j})\Big|_{(x,y)\in\Omega_{i,j}} \tag{19}$$

and

$$\mathbf{W}^{n,R}_{i+1/2,j} = \mathbf{W}^n(x_{i+1/2,j}, y_{i+1/2,j})\Big|_{(x,y)\in\Omega_{i+1,j}} \tag{20}$$

at interface $I_{i+1/2,j}$ using Eq. (11), we compute a reference state

$$\tilde{\mathbf{W}} = \left(\mathbf{W}^{n,L}_{i+1/2,j} + \mathbf{W}^{n,R}_{i+1/2,j}\right)\Big/2 \tag{21}$$

and linearize Eq. (16) about $\tilde{\mathbf{W}}$ to get the linearized Euler equations

$$\hat{\mathbf{W}}_t + \mathbf{A}_1\left(\tilde{\hat{\mathbf{W}}}\right)\hat{\mathbf{W}}_{\hat{x}} + \mathbf{A}_2\left(\tilde{\hat{\mathbf{W}}}\right)\hat{\mathbf{W}}_{\hat{y}} = 0, \tag{22}$$

where $\tilde{\hat{\mathbf{W}}}$ is $\tilde{\mathbf{W}}$ in the local coordinate system $(\hat{x},\hat{y})$. The eigenvalues of $\mathbf{A}_1(\tilde{\hat{\mathbf{W}}})$ are:

$$\begin{aligned}\lambda_1 &= \tilde{\hat{u}} - \tilde{a},\\ \lambda_2 &= \lambda_3 = \tilde{\hat{u}},\\ \lambda_4 &= \tilde{\hat{u}} + \tilde{a}\end{aligned} \tag{23}$$

with

$$\tilde{\hat{u}} = \tilde{u}\cos\theta + \tilde{v}\sin\theta, \quad \tilde{\hat{v}} = -\tilde{u}\sin\theta + \tilde{v}\cos\theta.$$

The matrix of corresponding right eigenvectors and its inverse are, respectively,

$$R\left(\tilde{\hat{\mathbf{W}}}\right) = \begin{bmatrix} -\frac{\tilde{\rho}}{\tilde{a}} & 1 & 0 & \frac{\tilde{\rho}}{\tilde{a}} \\ 1 & 0 & 0 & 1 \\ 0 & 0 & -1 & 0 \\ -\tilde{\rho}\tilde{a} & 0 & 0 & \tilde{\rho}\tilde{a} \end{bmatrix}, \quad R^{-1}\left(\tilde{\hat{\mathbf{W}}}\right) = \frac{1}{2}\begin{bmatrix} 0 & 1 & 0 & \frac{-1}{\tilde{\rho}\tilde{a}} \\ 2 & 0 & 0 & \frac{-2}{\tilde{a}^2} \\ 0 & 0 & -2 & 0 \\ 0 & 1 & 0 & \frac{1}{\tilde{\rho}\tilde{a}} \end{bmatrix}.$$

Multiplying Eq. (22) by $R^{-1}(\tilde{\hat{\mathbf{W}}})$ from the left we obtain the characteristic system

$$\hat{\mathbf{w}}_t + \begin{pmatrix} \tilde{\hat{u}} - \tilde{a} & 0 & 0 & 0 \\ 0 & \tilde{\hat{u}} & 0 & 0 \\ 0 & 0 & \tilde{\hat{u}} & 0 \\ 0 & 0 & 0 & \tilde{\hat{u}} + \tilde{a} \end{pmatrix} \hat{\mathbf{w}}_{\hat{x}} = \hat{\boldsymbol{S}}, \tag{24}$$

where

$$\hat{\mathbf{w}} = \begin{pmatrix} \hat{w}_1 \\ \hat{w}_2 \\ \hat{w}_3 \\ \hat{w}_4 \end{pmatrix} = \begin{pmatrix} \frac{1}{2}\left(-\frac{p}{\tilde{\rho}\tilde{a}} + u\cos\theta + v\sin\theta\right) \\ \rho - \frac{p}{\tilde{a}^2} \\ u\sin\theta - v\cos\theta \\ \frac{1}{2}\left(\frac{p}{\tilde{\rho}\tilde{a}} + u\cos\theta + v\sin\theta\right) \end{pmatrix} \tag{25}$$

are the characteristic variables and

$$\hat{\mathbf{S}} = \begin{pmatrix} \hat{s}_1 \\ \hat{s}_2 \\ \hat{s}_3 \\ \hat{s}_4 \end{pmatrix} = \begin{pmatrix} -\frac{1}{2}\tilde{a}\frac{\partial \hat{w}_3}{\partial \hat{y}} - \tilde{\hat{v}}\frac{\partial \hat{w}_1}{\partial \hat{y}} \\ -\tilde{\hat{v}}\frac{\partial \hat{w}_2}{\partial \hat{y}} \\ -\tilde{a}\frac{\partial \hat{w}_1}{\partial \hat{y}} + \tilde{a}\frac{\partial \hat{w}_4}{\partial \hat{y}} - \tilde{\hat{v}}\frac{\partial \hat{w}_3}{\partial \hat{y}} \\ \frac{1}{2}\tilde{a}\frac{\partial \hat{w}_3}{\partial \hat{y}} - \tilde{\hat{v}}\frac{\partial \hat{w}_4}{\partial \hat{y}} \end{pmatrix} \tag{26}$$

are the source terms.

3.2. The evaluation of $\underset{\frown}{\mathbf{U}}^{n+1/2}_{i+1/2,j}$

Unlike in [10], we solve Eq. (24) in terms of one-dimensional characteristics, and the multi-dimensional effects are considered by including the source terms $\hat{\mathbf{S}}$. The advantages of this approach are very simple, computationally efficient and easy to be implemented on general control volumes. In the present paper, Eq. (24) is solved using the following simple procedure:

$$\left(\underset{\frown}{\hat{w}_l}\right)^{n+1/2}_{i+1/2,j} = \hat{w}_l\left(x_{i+1/2,j} - \lambda_l(n_x)^n_{i+1/2,j}\Delta t/2, y_{i+1/2,j} - \lambda_l(n_y)^n_{i+1/2,j}\Delta t/2, t_n\right) + \hat{s}_l\Delta t/2, \quad (l = 1,2,3,4) \tag{27}$$

in which the source terms are frozen at t_n. When the piecewise linear reconstruction is considered, Eq. (27) yields

$$\begin{aligned} \left(\underset{\frown}{\hat{w}_l}\right)^{n+1/2}_{i+1/2,j} = {} & \frac{1+\mathrm{sign}(\lambda_l)}{2}\left\{(\hat{w}_l)^n_{i,j} + \left(\frac{\partial \hat{w}_l}{\partial x}\right)^n_{i,j}\left[x_{i+1/2,j} - x_{i,j} - \lambda_l(n_x)^n_{i+1/2,j}\Delta t/2\right]\right. \\ & \left. + \left(\frac{\partial \hat{w}_l}{\partial y}\right)^n_{i,j}\left[y_{i+1/2,j} - y_{i,j} - \lambda_l(n_y)^n_{i+1/2,j}\Delta t/2\right] + (\hat{s}_l)^n_{i,j}\Delta t/2\right\} \\ & + \frac{1-\mathrm{sign}(\lambda_l)}{2}\left\{(\hat{w}_l)^n_{i+1,j} + \left(\frac{\partial \hat{w}_l}{\partial x}\right)^n_{i+1,j}\left[x_{i+1/2,j} - x_{i+1,j} - \lambda_l(n_x)^n_{i+1/2,j}\Delta t/2\right]\right. \\ & \left. + \left(\frac{\partial \hat{w}_l}{\partial y}\right)^n_{i+1,j}\left[y_{i+1/2,j} - y_{i+1,j} - \lambda_l(n_y)^n_{i+1/2,j}\Delta t/2\right] + (\hat{s}_l)^n_{i+1,j}\Delta t/2\right\}. \end{aligned} \tag{28}$$

After computing $\underset{\frown}{\hat{\mathbf{w}}}^{n+1/2}_{i+1/2,j}$, the corresponding primitive variables $\underset{\frown}{\mathbf{W}}^{n+1/2}_{i+1/2,j}$ and conservative variables $\underset{\frown}{\mathbf{U}}^{n+1/2}_{i+1/2,j}$ can be easily derived.

3.3. The evaluation of $\mathbf{U}_{i+1/2,j}^{n+1/2}$

The contribution of the viscous effect to the numerical fluxes can be modeled by solving Eq. (15). In this way, the $\underset{\frown}{\mathbf{U}}_{i+1/2,j}^{n+1/2}$ can be corrected to get $\mathbf{U}_{i+1/2,j}^{n+1/2}$. Eq. (15) can be solved by applying the finite volume scheme on the control volume $\Omega_{i+1/2,j} = \Omega_{i,j} \cup \Omega_{i+1,j}$, which gives

$$\mathbf{U}_{i+1/2,j}^{n+1/2} = \underset{\frown}{\mathbf{U}}_{i+1/2,j}^{n+1/2} + \frac{\Delta t}{2(\Omega_{i,j} + \Omega_{i+1,j})} \left[\left(\sum_{k=1}^{4} \boldsymbol{\Psi}_k^{(V)^{(n)}} \Delta l_k \right)_{\Omega_{i,j}} + \left(\sum_{k=1}^{4} \boldsymbol{\Psi}_k^{(V)^{(n)}} \Delta l_k \right)_{\Omega_{i+1,j}} \right]. \tag{29}$$

This procedure is very efficient because the viscous fluxes in Eq. (29) are needed anyway to solve Eq. (7).

Using $\mathbf{U}_{i+1/2,j}^{n+1/2}$, the inviscid flux $\boldsymbol{\Psi}_{i+1/2,j}^{(E)^{\left(n+\frac{1}{2}\right)}}$ can be determined by

$$\boldsymbol{\Psi}_k^{(E)^{\left(n+\frac{1}{2}\right)}} = \boldsymbol{\Psi}_k^{(E)}\left(\mathbf{U}_k^{n+1/2}\right) = \mathbf{H}_k^{(E)}\left(\mathbf{U}_k^{n+1/2}\right) \cdot \mathbf{n}_k.$$

3.4. Remarks

Remark 1. We note that when the source terms are neglected in Eq. (28), the present scheme is reduced to the traditional grid-aligned finite volume scheme using a linearized Riemann solver. Therefore, the computation of the source terms is the only additional effort needed to account for the multi-dimensional effects, which makes the present scheme efficient with the costs being comparable to the grid-aligned finite volume schemes.

Remark 2. The present scheme is similar to the CTU scheme of Colella [3]. The differences between the present scheme and the CTU lie in a direct use of the equations in characteristic form to compute the numerical fluxes and the consideration of the multi-dimensional effects by the inclusion of the source terms in these equations. This practice makes it not necessary to solve additional Riemann problems in the transverse directions.

Remark 3. A distinctive feature of the present method is the consideration of the multi-dimensional effects due to viscous fluxes in the evaluation of the inviscid numerical fluxes when solving the Navier–Stokes equations. By analyzing the truncation errors of the present scheme shown in Eqs. (7) and (8), we found that when the viscous effects are considered, the present scheme is formally second order accurate on smooth enough meshes. However, when we omit the viscous contribution in evaluating the inviscid fluxes, the scheme will become temporally only first order accurate.

4. Numerical tests

In this section, several test cases are presented to verify the accuracy as well as the robustness of the present scheme. For the purpose of comparison, some test cases are also computed using the second order finite volume scheme based on the Roe's approximated Riemann solver [14]. In the implementation of the Roe scheme, the reconstruction procedure is the same as the present scheme, and the time-stepping algorithm is the two-stage, second order Runge–Kutta scheme [17].

4.1. Accuracy

We use the case of radially symmetric flow [9] to study the accuracy of the present numerical scheme. The initial condition has zero velocity and radially symmetric ρ and E which are expressed as

$$\rho(x,y,0) = E(x,y,0) = \begin{cases} 1 - 0.1(\cos(4\pi r) - 1) & \text{if } 0 < r < 0.5, \\ 1 & \text{if } r \geqslant 0.5, \end{cases}$$

where $r = \sqrt{x^2 + y^2}$. The problem is solved on a $[-1,1] \times [-1,1]$ plane domain.

We firstly consider the inviscid flow governed by the Euler equations. This problem is firstly solved on a 1280×1280 grid and the numerical solution is considered to be the "exact" solution. Then the numerical results on a sequence of grids are compared to the "exact" solution. Table 1 shows the computed error in each component in both the 1-norm and max-norm. The order of accuracy is estimated from the 40×40 and 80×80 grids. In these calculations, the average operator L is set to

$$L(a,b) = \frac{a+b}{2},$$

which means that limiter is not used. We can see that the results on the numerical accuracy of the present scheme compare favorably with similar test case presented in [9]. It should be noted that the lower accuracy of the max-norm can possibly be attributed to the non-smoothness in the initial condition at $r = 0.5$.

We then consider the viscous flow governed by the Navier–Stokes equations. The grids on which the computations are performed are the same as the inviscid case and the Reynolds number is 1000. In these computations, the solutions are advanced to $t = 0.45$ to avoid the influence of the viscous diffusion reaching the boundary. The rate of convergence are presented in Table 2. As in the inviscid case, the present scheme also shows second-order convergence for the viscous flow.

4.2. Robustness and resolution

To verify the robustness of the present scheme, three test cases are computed using the present scheme by solving the Euler equations, which are (1) Mach 20 inviscid supersonic flow around a circular cylinder [12]; (2) Mach 3 wind tunnel with a step [20]; and (3) double Mach reflection of a Mach 10 shock [20]. These test cases are difficult for Godunov-type schemes since the shock instability or the carbuncle phenomenon may occur when the grid aspect ratio is large or the grid is fine enough [13]. The numerical results of these test cases in terms of the density contours computed using the Roe scheme are presented in Figs. 3(a), 4(a) and 5(a). And the corresponding numerical results obtained using the present scheme are shown in Figs. 3(b), 4(b) and 5(b). The carbuncle instability of Roe scheme can be clearly seen in the numerical results. On the other hand, the present scheme dose not produce the carbuncle instability according to the numerical results shown in Figs. 3(b), 4(b) and 5(b). Recently, the carbuncle phenomenon was analyzed in [5] and it was concluded that

Table 1
Errors between the numerical solutions and the "exact solution" for the two-dimensional radially symmetric flow problem at $t = 0.5$

Grid	1-Norm errors			Max-norm errors		
	ρ	ρu	E	ρ	ρu	E
20×20	1.2593E − 3	9.7443E − 4	1.4495E − 3	4.6773E − 3	6.5207E − 3	6.1572E − 3
40×40	3.0164E − 4	2.2235E − 4	3.5156E − 4	2.6734E − 3	2.0598E − 3	3.6980E − 3
80×80	7.1893E − 5	5.1335E − 5	8.4470E − 5	7.5877E − 4	6.9428E − 4	1.0021E − 3
Order	2.07	2.11	2.06	1.82	1.57	1.88

The governing equations are the Euler equations. The errors are computed on three different grids. The order of accuracy is estimated from the two finest grids.

Table 2
Errors between the numerical solutions and the "exact solution" for the two-dimensional radially symmetric flow problem at $t = 0.45$

N	1-Norm errors			Max-norm errors		
	ρ	ρu	E	ρ	ρu	E
20	1.0359E − 3	8.8749E − 4	1.4495E − 3	7.8275E − 3	5.6520E − 3	1.0637E − 2
40	2.5342E − 4	1.8864E − 4	3.5156E − 4	2.6765E − 3	1.2312E − 3	3.6795E − 3
80	6.1197E − 5	4.1547E − 5	8.4470E − 5	5.6542E − 4	2.6419E − 4	7.7103E − 4
Order	2.05	2.18	2.06	2.24	2.22	2.25

The governing equations are the Navier–Stokes equations. The errors are computed on three different grids. The order of accuracy is estimated from the two finest grids.

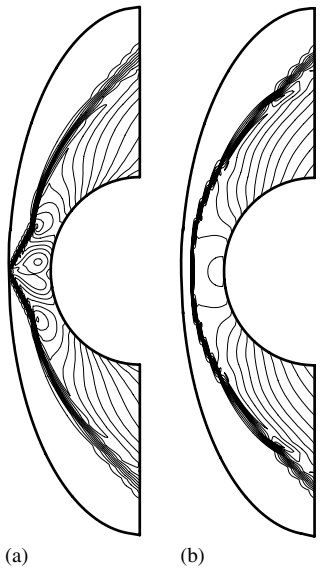

Fig. 3. Density contours of supersonic inviscid flow around a blunt body at $M_\infty = 20$. There are 20 cells in the radial direction and 720 cells in the circumferential direction. The numerical results are obtained with: (a) the second order Roe scheme; (b) the present scheme.

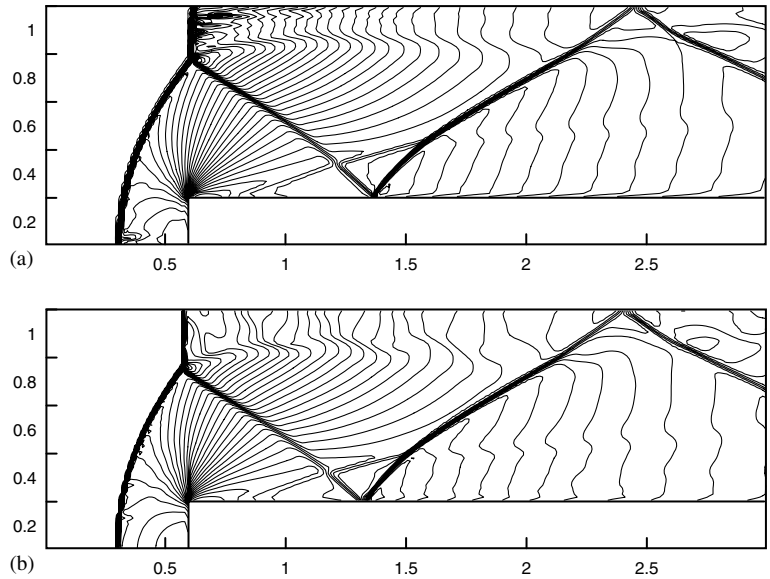

Fig. 4. Mach 3 wind tunnel with a step. The numerical results in terms of the density contours at $t = 4.0$ on a 200×80 uniform grid are obtained with: (a) the second order Roe scheme; (b) the present scheme.

the numerical carbuncle phenomenon was due to an unconditional instability of the underlying mean flow. Therefore, it is suggested that the use of a genuinely multi-dimensional upwind scheme alone does not help for eliminating the carbuncle phenomenon [16]. However, the present numerical experiment shows that the inclusion of multi-dimensional effects seems to be beneficial in improving the robustness of the numerical scheme and curing the carbuncle instability in some well-known test cases.

The second order accuracy of the present scheme for problems with smooth solution has been verified in Section 4.1. When the shock waves are present in the flow fields, another concern is the resolution to the shock

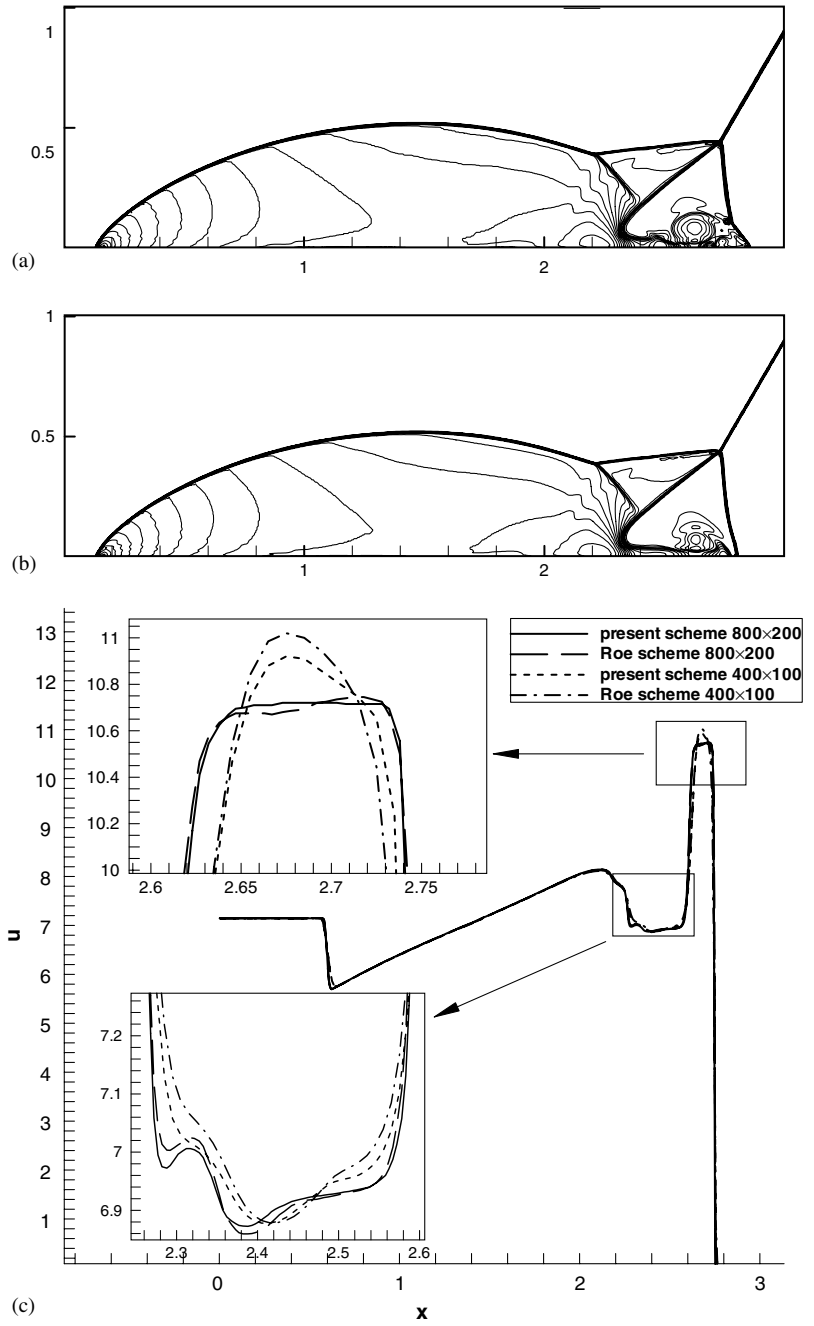

Fig. 5. Double Mach reflection problem. The numerical results at $t = 0.2$ are presented. (a) Density contours predicted by the second order Roe scheme on a 800×200 uniform grid. (b) Density contours predicted by the present scheme on a 800×200 uniform grid. (c) The distribution of u along a horizontal line at $y = 0.34$ predicted by the second order Roe scheme and the present scheme on a 800×200 grid as well as a 400×100 grid.

waves. To verify the resolution property of the present scheme, the u-component of the velocity distribution along the line $y = 0.34$ (away from the carbuncle instability region) of the double Mach reflection problem is depicted in Fig. 5(c). The numerical results obtained using the present scheme and the second order Roe scheme on a 800×200 grid as well as a 400×100 grid are shown in this figure. It can be seen that on the 800×200 grid, the present scheme and Roe scheme predict similar results with the present scheme capturing

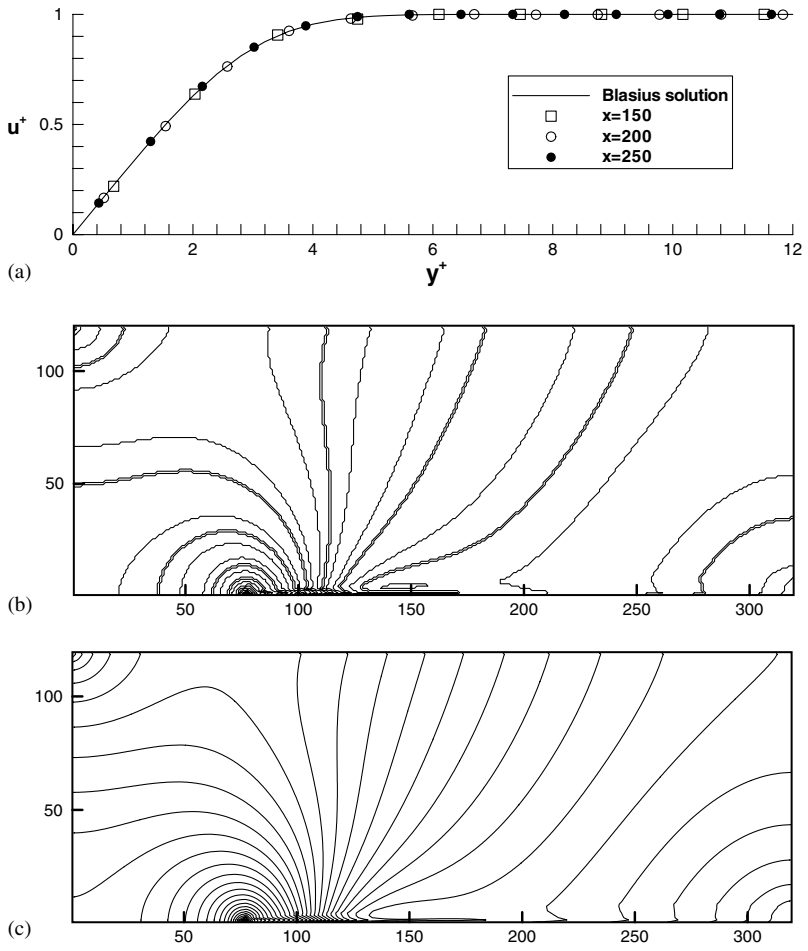

Fig. 6. The numerical solution for the 2D laminar boundary layer problem on a 320×120 uniform grid. (a) $u^+ \sim y^+$ distribution at different locations of the flat plate computed by the present scheme. The output locations are: □, $x = 150$; ●, $x = 200$; ○, $x = 250$. The solid line is the Blasius solution. (b) Pressure contours (max = 71.4, min = 71.8, $\Delta = 0.01$) computed using the second order Roe scheme. (c) Pressure contours (max = 71.4, min = 71.8, $\Delta = 0.01$) computed using the present scheme.

the shock waves as well as the contact discontinuity slightly sharper than the Roe scheme. On the 400×100 grid, results of the present scheme are closer to the finer grid solution than those of the Roe scheme.

4.3. Viscous flow simulation

In this section, we apply the present scheme to solve the flat plate boundary layer problem which is a more practical viscous flow case than the case in Section 4.1. The free stream Mach number is $M_\infty = 0.3$, and the Reynolds number defined by $Re = \frac{\rho_\infty u_\infty L}{\mu_\infty}$ is 3×10^4 where L is the length of the plate. Fig. 6(a) plots the $u^+ \sim y^+$ distributions at different locations computed by the present scheme using a 320×120 uniform grid with $\Delta x = 1.0$ and $\Delta y = 1.0$. It can be seen that the numerical result of the present scheme agrees very good with the Blasius solution. According to the numerical results in [21], the performance of the second order Van Leer scheme [20] is rather poor on the same grid. We have also obtained similar results which are however not shown here. The second order Roe scheme can capture the boundary layer as good as the present scheme, but the fluctuations in the pressure field are observed in Fig. 6(b), especially near the leading edge of the plate where the flow singularity exists. On the other hand, the present scheme predicts a very smooth pressure field which can be seen in Fig. 6(c).

5. Conclusion

In this paper, a second order multi-dimensional upwind finite volume scheme for solving compressible Euler and Navier–Stokes equations is presented. In this scheme, the multi-dimensional effect is accounted for by solving full governing equations on cell interfaces to evaluate the inviscid numerical fluxes. When the Navier–Stokes equations are concerned, the contribution of the viscous terms on the inviscid numerical fluxes is also included. The proposed scheme is designed to apply on general shape control volumes for solving both Euler and Navier–Stokes equations with the efficiency being comparable to the grid-aligned finite volume schemes. The numerical test cases indicate that the present scheme is second order accurate and outperforms some well known grid-aligned finite volume scheme in terms of robustness and resolution to flow discontinuities.

Acknowledgments

This work was supported by Project-10572075 of NSFC and Project-2001CB409604 of China NKBRSF. We thank the referee of this paper for the valuable suggestions to improve the quality of this paper.

References

[1] S. Billet, E.F. Toro, On WAF-type schemes for multi-dimensional Riemann solver for Euler equations of gas dynamics, J. Comput. Phys. 130 (1997) 1–24.
[2] M. Brio, A.R. Zakharian, G.M. Webb, Two-dimensional Riemann solver for Euler equations of gas dynamics, J. Comput. Phys. 167 (2001) 177–195.
[3] P. Collela, Multi-dimensional upwind methods for hyperbolic conservation laws, J. Comput. Phys. 87 (1990) 171.
[4] H. Deconinck, H. Paillère, R. Struijs, P. Roe, Multi-dimensional upwind schemes based on fluctuation splitting for systems of conservation laws, Comput. Mech. 11 (1993) 323.
[5] M. Dumbser, J. Moschetta, J. Gressier, A matrix stability analysis of the carbuncle phenomenon, J. Comput. Phys. 197 (2004) 647–670.
[6] M. Fey, Multi-dimensional upwinding. Part II. Decomposition of the Euler equations into advection equations, J. Comput. Phys. 143 (1998) 181–199.
[7] A. Kurganov, G. Petrova, A third-order semi-discrete genuinely multi-dimensional central scheme for hyperbolic conservation laws and related problems, Numer. Math. 88 (2001) 683–729.
[8] J.O. Langseth, R.J. LeVeque, A wave propagation method for three-dimensional hyperbolic conservation laws, J. Comput. Phys. 165 (2000) 126–166.
[9] R.J. LeVeque, Wave propagation algorithms for multi-dimensional hyperbolic systems, J. Comput. Phys. 131 (1997) 327–353.
[10] M. Lukáčová-Medvid'ová, J. Saibertová, G. Warnecke, Finite volume evolution Galerkin methods for nonlinear hyperbolic systems, J. Comput. Phys. 183 (2002) 533–562.
[11] S. Noelle, The MOT-ICE: a new high-resolution wave-propagation algorithm for multi-dimensional systems of conservative laws based on Fey's method of transport, J. Comput. Phys. 164 (2000) 283–333.
[12] M. Pandolfi, D. D'Ambrosio, Numerical instabilities in upwind methods: analysis and cures for the "carbuncle" phenomenon, J. Comput. Phys. 166 (2001) 271–301.
[13] J. Quirk, A contribution to the great Riemann solver debate, Int. J. Numer. Meth. Fluid Dyn. 18 (1994) 555.
[14] P.L. Roe, Approximate Riemann solvers, parameter vectors, and difference schemes, J. Comput. Phys. 43 (1981) 357.
[15] P.L. Roe, Discrete models for the numerical analysis of time-dependent multi-dimensional gas dynamics, J. Comput. Phys. 63 (1986) 458–476.
[16] K. Sermeus, H. Deconinck, Solution of steady Euler and Navier–Stokes equations using residual distribution schemes, in: 33rd Computational Fluid Dynamics Course, VKI Lecture Series 2003-05, 2003.
[17] C.-W. Shu, S.J. Osher, Efficient implementation of essentially non-oscillatory shock capturing schemes, J. Comput. Phys. 77 (1988) 439–471.
[18] E. Toro, Riemann Solvers and Numerical Methods for Fluid Dynamics, Springer-Verlag, New York, 1999.
[19] B. van Leer, Progress in multi-dimensional upwinding, ICASE Report 92-43, 1992.
[20] P. Wood, P. Colella, Numerical simulations of two-dimensional fluid flow with strong shocks, J. Comput. Phys. 54 (1984) 115.
[21] K. Xu, Z. Li, Dissipative mechanism in Godunov-type schemes, Int. J. Numer. Meth. Fluids 37 (2001) 1–22.